

Characterization and Control of the Compromise Between Tensile Properties and Fracture Toughness in a Quenched and Partitioned Steel



ZHIPING XIONG, PASCAL J. JACQUES, ASTRID PERLADE,
and THOMAS PARDOEN

The enhancement of the fracture toughness is essential for opening the possible range of applications of advanced high-strength steels, while the focus in the literature is primarily on the strength–ductility compromise. A high fracture toughness is indeed needed for energy absorbing components as well as to limit edge cracking sensitivity during part forming. This study investigates the tensile properties and the fracture toughness of various quenched and partitioned microstructures. The fracture resistance is evaluated using double-edge notched tension tests. While the uniform elongation continuously increases with the retained austenite (RA) fraction, the fracture toughness shows a maximum at intermediate RA content. For the highest amount of RA, the relatively low fracture toughness is mainly attributed to the formation of brittle necklace of fresh blocky martensite in the fracture process zone due to a high stress triaxiality, inducing an intergranular fracture mode. For intermediate RA fraction, the RA morphology evolves from blocky to film type, leading to a transition from intergranular to ductile fracture mode, and the RA-to-martensite transformation contributes to a higher total work of fracture compared to tempered martensitic steel. A proper control of both the amount and morphology of RA during microstructure design is thus essential to generate the best compromise between tensile properties and fracture toughness.

<https://doi.org/10.1007/s11661-019-05265-2>

© The Minerals, Metals & Materials Society and ASM International 2019

I. INTRODUCTION

SINCE the first proposal of quenched & partitioned (Q & P) process by Speer *et al.*,^[1] the family of Q & P steels, which belongs to the third generation of advanced high-strength steels (AHSSs), has received major attention in particular regarding the understanding of the microstructure evolution and the improvement of mechanical properties.^[2] In addition, the Q & P process has been successfully applied in the conventional industrial steel processes such as for AISI 430-type stainless steel,^[3] austempered ductile cast iron,^[4] medium carbon bar steels,^[5] and hot stamping steels.^[6] The Q & P process involves a quenching stage from the austenite or

austenite and ferrite domain where martensite forms and a following partitioning stage where carbon redistributes between martensite and austenite,^[7] leading to the retention of some amount of austenite at room temperature named retained austenite (RA).^[5,8]

Q & P steels combine high ultimate tensile strength (UTS) and large ductility owing to the combined presence of tempered martensite and RA as demonstrated by many works focusing on the tensile properties.^[9–11] Tempered martensite provides high strength, while the presence of RA improves ductility through enhanced progressive work hardening resulting from the transformation-induced plasticity (TRIP) effect. The amount of RA can be controlled *via* the adjustment of the quenching temperature and partitioning time at different partitioning temperatures.^[7,9–11] In turn, the tensile properties are adjustable by tuning the amount, morphology, and stability of RA, leading to a wide range of properties.^[12,13]

Regarding the cracking resistance of Q & P steels and other steels in general, the tendency in the literature is often to use the product of UTS and total elongation (TE) as a fracture indicator. However, this link with fracture toughness and tensile properties can be misleading. For AHSSs, higher ductility does not

ZHIPING XIONG, PASCAL J. JACQUES, and THOMAS PARDOEN are with the Université catholique de Louvain, Institute of Mechanics, Materials and Civil Engineering, IMAP, 1348 Louvain-la-Neuve, Belgium. Contact e-mail: zhiping.xiong@uclouvain.be; zuileniwota@126.com ASTRID PERLADE is with the ArcelorMittal Global R&D Maizières Products, Voie Romaine, BP 30320, 57283 Maizières-lès-Metz Cedex, France.

Manuscript submitted January 6, 2019.

necessarily mean higher flangeability as for other ductile steels.^[14] For instance, although DP 1000 steel (ferrite-martensite Dual-Phase steel having a UTS of ~ 1000 MPa) has a larger TE than CP 1000 steel (Complex-Phase steel having a UTS of ~ 1000 MPa mainly consists of bainite and martensite), DP 1000 steel shows a smaller hole expansion ability because of a higher work hardening in the DP steel due to soft ferrite and hard martensite, and a lower work hardening in the CP steel due to the compatible deformation between bainite and martensite.^[15] Edge cracks have been repeatedly reported during AHSSs' application (such as stretch flanging and hole expansion) for automotive components, indicating that the fracture resistance is an important property for AHSSs not only for structural applications but also regarding formability. The main reasons explaining the observed discrepancy between the UTS \times TE product and cracking resistance include firstly the large difference between the stress state at the crack tip compared to uniaxial tension and, secondly, the limited physical/mechanical meaning of the TE, which is not a true measurement of the fracture strain. The high stress triaxiality at the crack tip can significantly modify the damage process as well as it can change the transformation rate in the case of TRIP-sensitive materials. Fracture mechanics, being the appropriate rigorous framework to characterize the fracture toughness, must thus be used to address cracking resistance of AHSSs.^[16,17]

Fracture toughness in AHSSs has been characterized in a few studies using double-edge notched tension (DENT) specimens.^[18–20] This geometry has the advantage of limiting warping and buckling effects due to tensile transverse stress between notches. Jacques *et al.*^[20] and Lacroix *et al.*^[17] investigated the effect of RA and martensite fractions on the fracture resistance of low-alloyed multi-phase TRIP steels and ferrite-martensite DP steels using DENT specimens, involving as well analysis of the fracture mechanisms. For Q & P steels, de Diego-Calderón *et al.*^[18] found, for DENT specimens, that the initial fracture toughness was not significantly affected by the RA fraction, while the total crack resistance was significantly improved by an increase in RA fraction. Conversely, Wu *et al.*^[19] demonstrated that less stable RA improves the fracture toughness, while the fracture toughness decreases with more stable RA. Furthermore, Casellas *et al.*^[16] successfully established a proportional relationship between the hole expansion ratio and the fracture toughness of AHSSs. Noticeably, a systematic investigation of the evolution of the fracture resistance with microstructure is essential and necessary. In the present study, tensile properties and fracture resistance, respectively, characterized using dog-bone tensile samples and DENT specimens of Q & P steels were analyzed in terms of microstructure evolution with quenching temperature. Based on the understanding of the relationship between the microstructure, failure micro-mechanisms and austenite stability, a new suggestion for microstructure optimization is proposed in terms of a trade-off between tensile properties and fracture resistance.

II. EXPERIMENTAL METHODS

A 0.3C-2.5Mn-1.5Si-0.8Cr (wt pct) steel grade was systematically studied in terms of microstructure and mechanical properties using a two-step Q & P process. Cold-rolled strips 1.25 mm in thickness were provided by ArcelorMittal Global R&D Maizières Products (France). As shown in Figure 1(a), samples were austenitized at 900 °C for 160 seconds using a fluidized bed furnace, transferred to a salt bath furnace and held at different quenching temperatures for 60 seconds, and transferred again to another salt bath furnace and held at 400 °C for 500 seconds, followed by water quenching. Under the assumption of full partitioning between the martensitic laths and the austenite prior to final quenching to room temperature, the volume fraction of martensite (f) can be calculated according to the Koistinen–Marburger relationship^[21]:

$$f = 1 - \exp[-\alpha_m(M_S - T)], \quad [1]$$

where M_S is the martensite transformation start temperature (310 °C calculated using Eq. [2] of Reference 21), T is the quenching temperature, and α_m is related to the concentrations of the different alloying elements (0.019 K⁻¹ calculated using Eq. [4] of Reference 21). Following this, the microstructure components evolving with the quenching temperature are predicted as illustrated in Figure 1(b). Based on this, three quenching temperatures equal to 211 °C, 190 °C, and 159 °C (Figure 1) were selected (hereafter, respectively, referred as to QT 211, QT 190, and QT 159), which would result in a decreasing volume fraction of RA. In comparison, tempered martensitic steel (referred to QT 25) was also processed by directly quenching from austenitization temperature to room temperature followed by tempering at 400 °C for 500 seconds.

The samples for microstructure characterization were cut perpendicular to the rolling direction, and parallel to the rolling and transverse directions for X-ray diffraction (XRD). The samples were mounted, polished down to 1 μ m followed by colloidal silica suspension (OP-S) polishing and finally etched using 2 vol pct nital. The microstructure was characterized using a field emission gun-scanning electron microscope (SEM, ultra 55) at a voltage of 15 kV, a working distance of 10 mm and an aperture size of 30 μ m. The RA fraction was measured using XRD with Co K α radiation over a range of $2\theta = 55$ –110 deg at a step size of 0.01 deg and a step time of 5 seconds. It was calculated using the integrated intensities of two austenite peaks {(200) and (220)} and two ferrite peaks {(200) and (211)} based on direct comparison method. The average carbon content of RA was estimated from the mean lattice parameter using the following relationship^[2]:

$$a_\gamma = 0.3556 + 0.00453x_C + 0.000095x_{Mn} + 0.0006x_{Cr}, \quad [2]$$

where a_γ is the austenite lattice parameter (nm) determined from the experimental mean scattering angle,^[22] while x_C , x_{Mn} , and x_{Cr} represent concentrations (in wt pct) of carbon, manganese, and chromium,

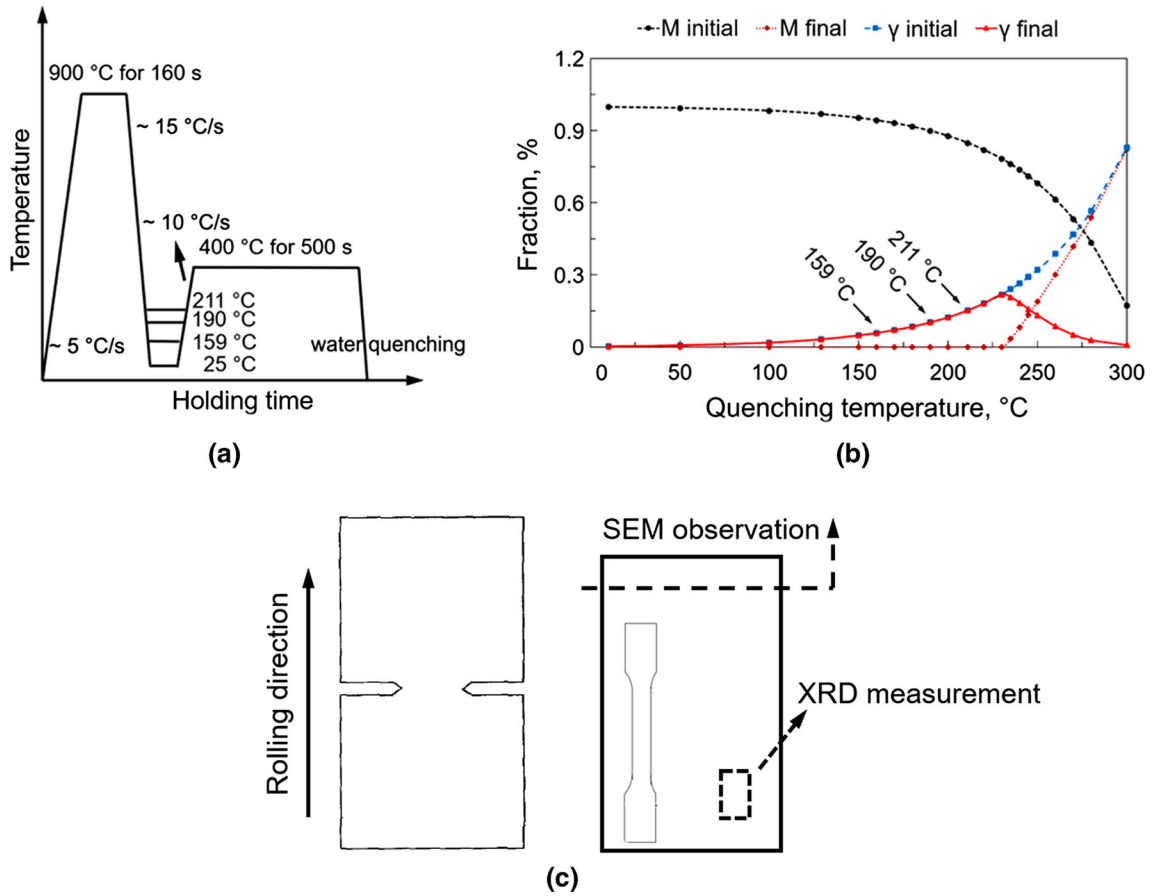


Fig. 1—(a) Illustration of the heat treatment schedules, (b) predicted microstructure components for the studied steel as a function of quenching temperature, with assumption of full partitioning between the martensitic laths and the retained austenite prior to final quenching to room temperature. M stands for martensite and γ for austenite and (c) illustration of cutting samples.

respectively. The concentrations of substitutional alloying elements were approximately equivalent to nominal steel composition.

As illustrated in Figure 1(c), DENT specimens of $100 \times 50 \times 1.25 \text{ mm}^3$ were machined with the notches perpendicular to the rolling direction. The 15-mm-long notch on each side was produced by electric discharge machining (14 mm) followed by fresh razor blade sharpening (over a length $\approx 1 \text{ mm}$), resulting in a ligament of 20 mm and an initial crack opening of $\sim 50 \mu\text{m}$. Dog-bone tensile samples were machined with a gauge length of 26 mm parallel to rolling direction and a width of 6 mm parallel to the transverse direction. The tensile tests were carried out under a displacement controlled mode using a screw-driven universal testing machine (Zwick, the load capacity is 250 kN) at a cross-head speed of 1 mm min^{-1} . The fracture surfaces of broken specimens were examined by SEM. The true fracture stress (σ_f) was approximately evaluated by dividing the force by the cross-sectional area at the fracture point, while the true fracture strain (ϵ_f) was estimated as follows:

$$\epsilon_f = \ln\left(\frac{A_0}{A}\right), \quad [3]$$

where A_0 and A are the initial and current area of cross section. For DENT test, J -integral was calculated from load–displacement curve as proposed by Rice *et al.*^[23]:

$$J_{\text{Rice}} = \frac{K_I^2}{E} + \frac{1}{l_0 t_0} \left(2 \int P du_p - P u_p \right), \quad [4]$$

$$K_I = \frac{P \sqrt{\frac{\pi a_0}{2w_0}}}{t_0 \sqrt{w_0} \sqrt{1 - \frac{a_0}{w_0}}} \times \left(1.122 - 0.561 \left(\frac{a_0}{w_0} \right) - 0.205 \left(\frac{a_0}{w_0} \right)^2 + 0.471 \left(\frac{a_0}{w_0} \right)^3 + 0.19 \left(\frac{a_0}{w_0} \right)^4 \right), \quad [5]$$

where K_I is the stress intensity factor (calculated using Eq. [5]^[24]), E is the Young's modulus, P is the applied load, u_p is the plastic displacement, l_0 is the ligament, t_0 is the thickness, a_0 is the half of initial crack length, and w_0 is the half-width of the plate.

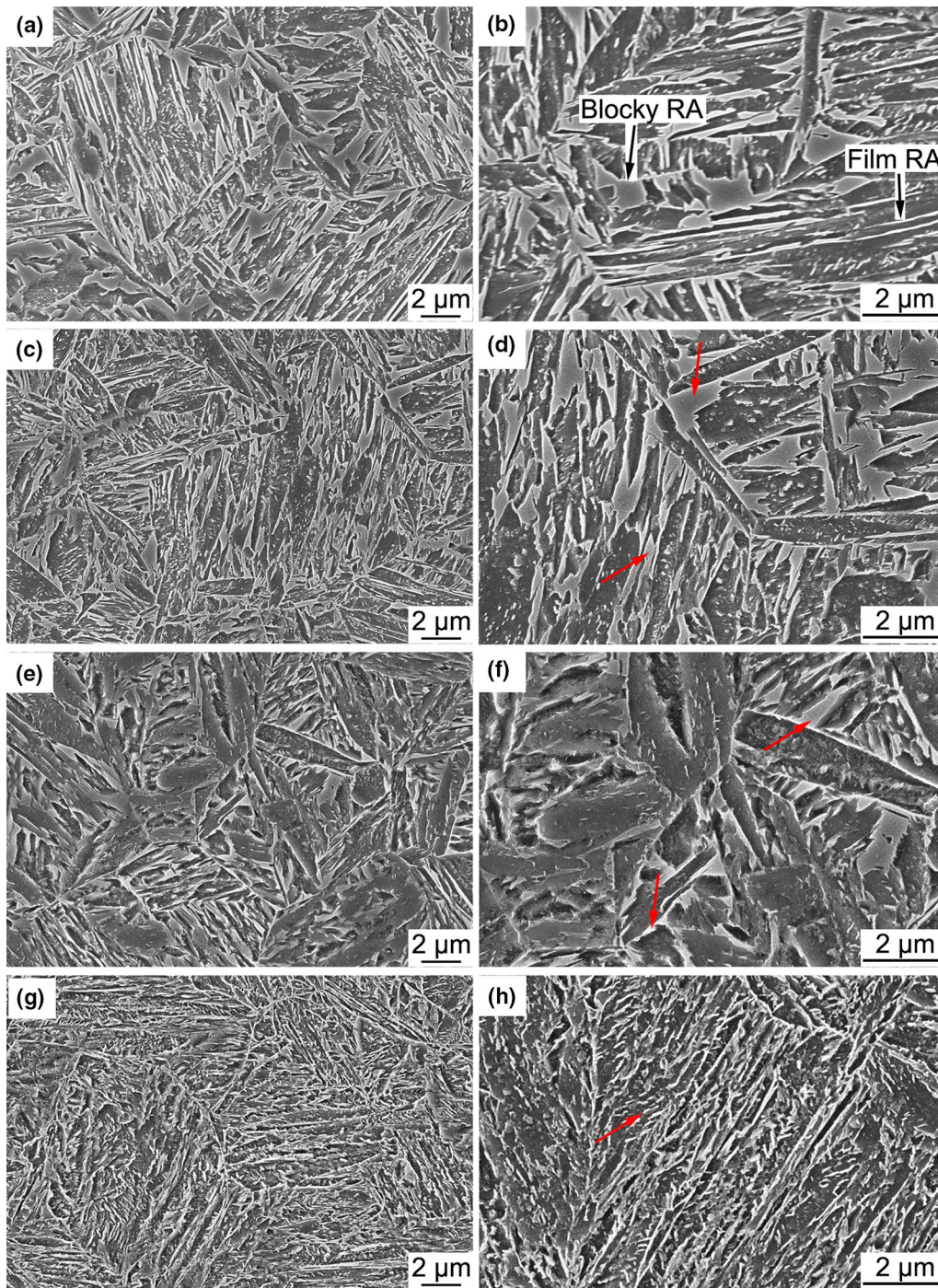


Fig. 2—Microstructures of (a, b) QT 211, (c, d) QT 190, (e, f) QT 159, and (g, h) QT 25. RA is the retained austenite under either blocky or film-type morphology.

III. RESULTS

A. Microstructure Characterization

Figures 2 and 3 illustrate the microstructures and the evolution of the RA fraction and its carbon content (measured by XRD) with quenching temperature, respectively. Generally, the microstructure consists of martensitic packets with dispersed RA and carbides. After quenching to 211 °C (QT 211), many blocky RA

islands distribute along martensitic packet boundaries with a necklace topology, while film RA grains intercalate between martensitic laths (Figures 2(a) and (b)). With a decrease in quenching temperature from 211 °C to 159 °C, the RA fraction decreases from 17.6 to 11.2 pct, while the carbon content increases from 0.90 to 0.98 wt pct (Figure 3). Due to an increase in the fraction of martensitic laths related to a lower quenching temperature (Figure 1), the amount of blocky RA along

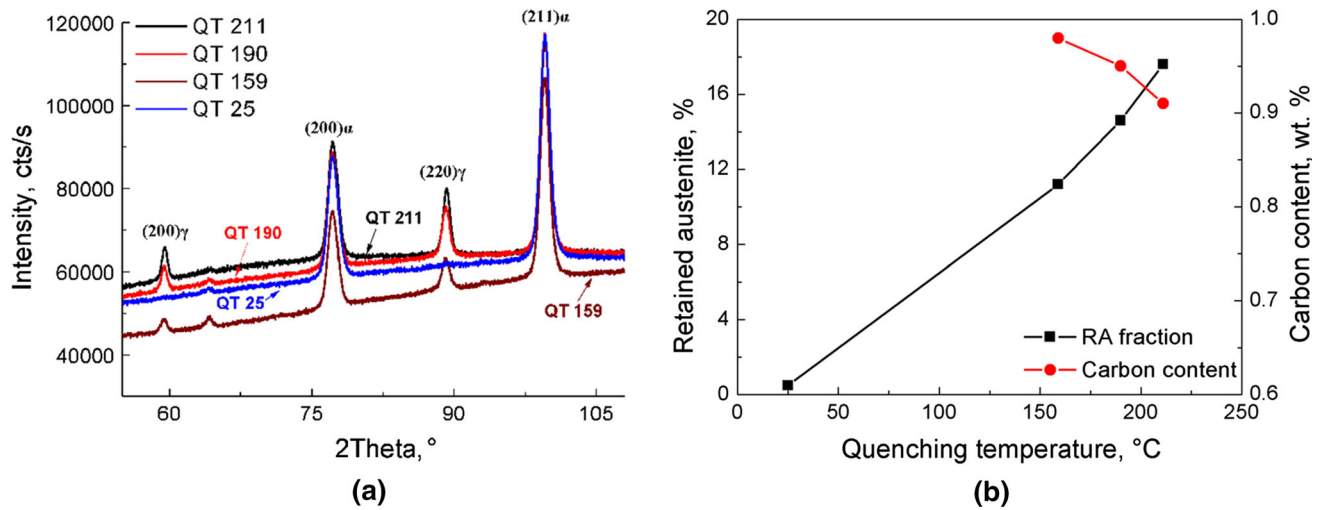


Fig. 3—(a) X-ray diffractograms after quenching at different temperatures and (b) corresponding evolution of retained austenite fraction and its carbon content with quenching temperature.

the boundaries of the martensitic packets decreases and the film RA between martensitic laths becomes dominant (Figures 2(a) through (f)). In tempered martensitic steel (QT 25), the amount of RA is less than 1 pct (Figure 3). In contrast, many carbides precipitate (for example, indicated by the arrow) along martensitic packet boundaries and inside martensitic laths (Figures 2(g) and (h)). The measured RA fractions follow the tendency of the predicted RA fractions with a decrease of quenching temperature. However, the values retrieved from experiments and predictions are different predominantly because the model does not consider the carbide precipitation in the martensite and the inhomogeneities in the microstructure such as the distribution between the blocky and film morphology of the RA.

B. Uniaxial Tensile Properties

The true stress–true strain curves (solid lines) are given in Figure 4(a). The curves are linearly extrapolated from the necking point to ϵ_f (dashed lines). Tensile properties listed in Table I are retrieved from the engineering and true stress–strain curves, respectively. The yield strength (YS) is defined using a 0.2 pct offset. The tempered martensitic steel (QT 25) has the highest strength and lowest elongation due to its fully martensitic structure. In addition, it exhibits the largest ϵ_f and the highest $\sigma_f \times \epsilon_f$ product. For Q & P steel, with an increase in quenching temperature, the YS and UTS (Table I) decrease due to a decreasing amount of martensite, while the uniform elongation (UE), ϵ_f (Figure 4(d)), and the $\sigma_f \times \epsilon_f$ product increase. However, the TE and the UTS \times TE product (Table I) do not continuously increase when increasing quenching temperature. The QT 159 sample has larger values than the QT 190 sample. This suggests that the TE has relatively little meaning and that only UE and ϵ_f are worth attention. The enhancement of UE and ϵ_f results from an increase in the amount of RA (Figure 3). This is

due to the increased TRIP effect, which in turn provides a better resistance to plastic localization. As shown in Figure 4(c), the strain hardening exponent first rapidly decreases in the elastoplastic transition regime. Then, it increases predominantly because of continuous austenite-to-martensite transformation.^[25] The strain hardening exponent is larger for a larger amount of RA (quenching temperature), allowing the necking point to be postponed to a true strain of ~ 0.11 for the QT 211 sample (Figure 4(c)) in comparison to a true strain of ~ 0.04 for the QT 25 sample.

Figure 5 illustrates the fracture surfaces of the tensile specimens for different quenching temperatures. All Q & P steels exhibit a ductile fracture mechanism with bimodal dimple size distribution (Figures 5(a) through (c)). Examples of small dimples are shown in the insets of Figures 5(a) and (c). In QT 211 sample, the spacing between large dimples and between small dimples is, respectively, equal to 2.0 ± 0.7 and $0.38 \pm 0.12 \mu\text{m}$. These dimensions correspond to the distance of $1.6 \pm 0.6 \mu\text{m}$ between blocky RA islands and of $0.37 \pm 0.12 \mu\text{m}$ between martensitic laths, respectively. It indicates that large and small dimples nucleate at the boundaries of blocky RA islands and of martensitic laths, respectively. It means that the carbides in the martensitic laths do not seem to significantly affect the damage mechanisms.^[10]

Several ductile tearing cracks are also observed (indicated by the arrows in Figure 5(a)) but the size is limited. The observed ductile tearing here probably originates from the coalescence of voids. With a decrease in quenching temperature down to 159 °C (QT 159), the dimples are still predominant. The spacing between large dimples increases up to $3.1 \pm 1.3 \mu\text{m}$ (Figures 5(b) and (c)) due to a decreased amount of blocky RA islands (Figure 2), while the spacing between small dimples remains unchanged due to similar arrangement of martensitic laths. In addition, the number and the size of the ductile tearing cracks

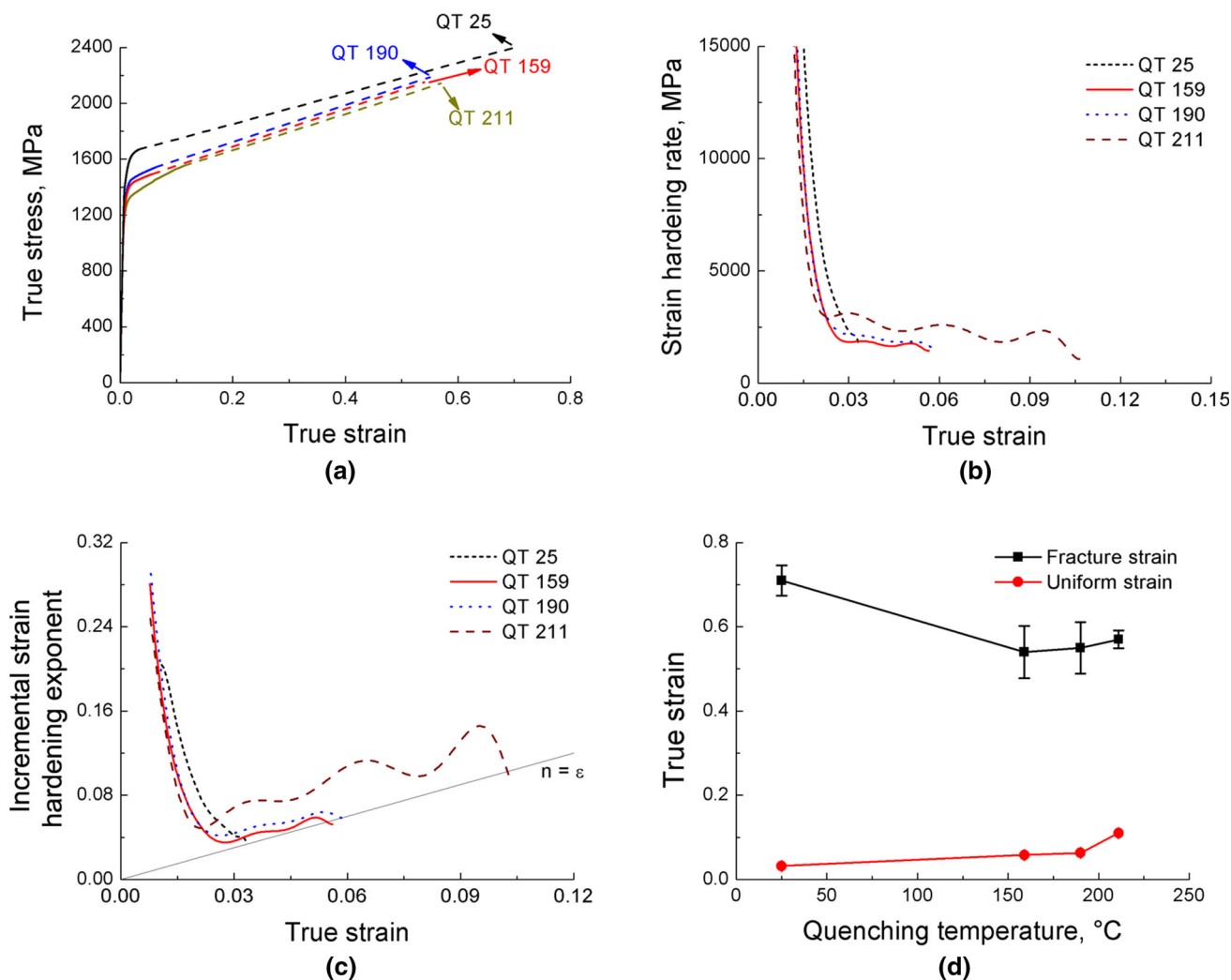


Fig. 4—(a) True stress–true strain curves, (b) strain hardening rate vs true strain, (c) incremental strain hardening exponent vs true strain, and (d) fracture strain and uniform strain as a function of quenching temperature.

increase, which explains the decrease in ϵ_f . The ductile tearing probably reduced ductility with surface topography showing shear damage mechanisms. Tempered martensitic steel (QT 25, Figure 5(d)) shows many small dimples that nucleate at carbides (Figure 2(g)). Some large ductile tearing cracks are also observed.

C. Double-Edge Notched Tension Tests

The load–displacement curves corresponding to the tests on DENT samples are given in Figure 6(a). The different curves indicate that crack initiation occurs before the maximum force is attained. The crack initiation is determined by a small disturbance in the curve (pointed by an arrow in the inset of Figure 6(a)) accompanied with a cracking sound during DENT test. With a decrease in quenching temperature from 211 °C to 159 °C, the force at crack initiation and the maximum force both increase (Figure 6(b)), while the work of fracture ($\int P du$, corresponding to crack initiation, maximum force and full response in Figure 6(c)), and

fracture toughness at crack initiation (Figure 6(d)) also increase. Surprisingly, the tempered martensitic steel (QT 25) has higher crack initiation and maximum forces than QT 211 sample, while the former exhibits a lower work of fracture (corresponding to crack initiation, maximum force, and full response) and fracture toughness at crack initiation. These differences presumably come from the counterbalance between the assistance of fresh martensite (transformed from RA) to induce crack initiation and the energy consumption by RA-to-martensite transformation.

The evolution of the fracture surface with quenching temperature is shown in Figure 7. The fracture surfaces are very different from uniaxial tension (Figure 5). At the crack initiation, QT 211 sample exhibits intergranular fracture with cracks decorating the boundaries of the facets and with very few dimples (Figure 7(a)). The “crack” here indicates what is observed in the fracture surfaces. The similar equivalent circled diameter of the facets ($10.9 \pm 3.8 \mu\text{m}$) and martensitic packets ($10.8 \pm 3.9 \mu\text{m}$) indicates that this intergranular fracture

Table I. Tensile Properties of Studied Steel Subjected to Different Quenching Temperatures

	Yield Strength (MPa)	Ultimate Tensile Strength (MPa)	Uniform Elongation (Pct)	Total Elongation (Pct)	Product of Ultimate Tensile Strength and Total Elongation (MPa Pct)	Fracture Strain	Fracture Stress (MPa)	Product of Fracture Stress and Fracture Strain (MPa Pct)
QT 211	1145 ± 24	1408 ± 22	11.8 ± 0.25	17.8 ± 0.55	24,993	0.57 ± 0.02	2142 ± 98	1220
QT 190	1211 ± 6	1448 ± 1	6.5 ± 0.05	12.6 ± 0.01	18,248	0.55 ± 0.06	2186 ± 133	1202
QT 159	1227 ± 17	1437 ± 26	6.1 ± 0.15	13.2 ± 0.35	18,892	0.54 ± 0.06	2094 ± 107	1131
QT 25	1441 ± 26	1631 ± 17	3.6 ± 0.15	8.1 ± 0.30	13,214	0.71 ± 0.04	2410 ± 166	1711

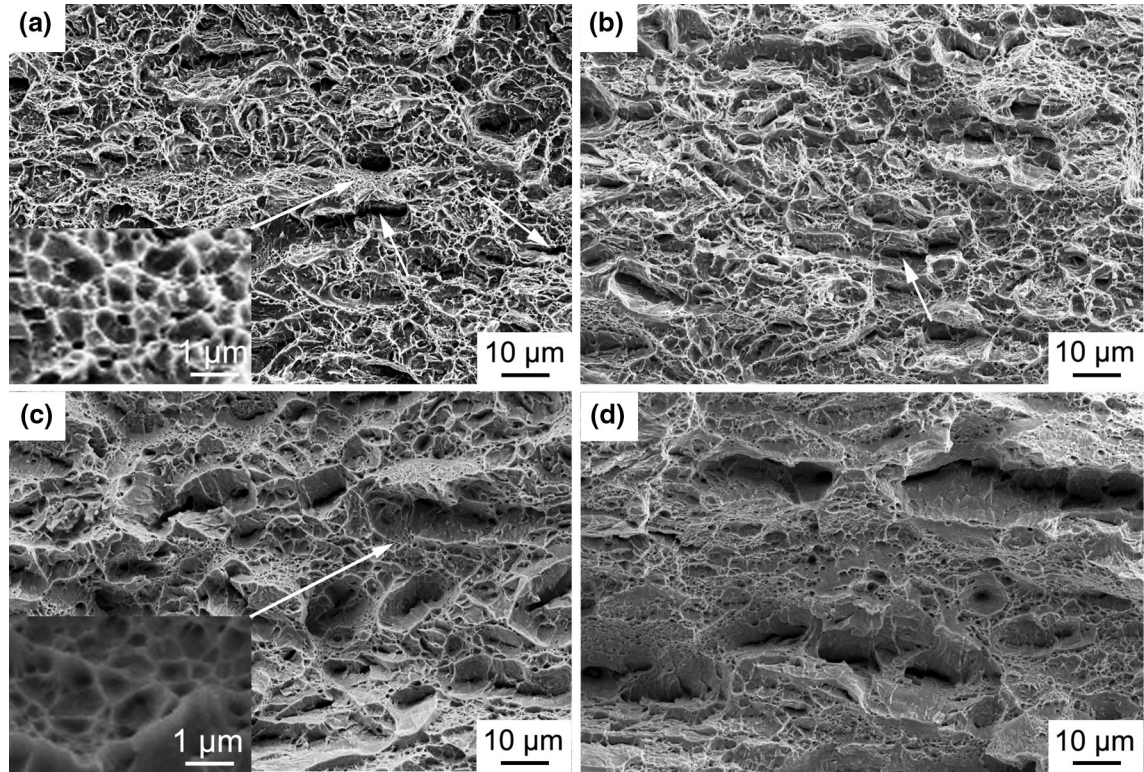


Fig. 5—Fracture surfaces after uniaxial tension: (a) QT 211, (b) QT 190, (c) QT 159, and (d) QT 25.

mechanism takes place along the boundaries of the martensitic packets. QT 190 sample (Figure 7(c)) has similar fracture surface as QT 211 sample but more dimples and fewer cracks are observed. Noticeably, QT 159 sample shows a completely different fracture surface where dimples are dominant instead of facets (Figure 7(e)). In contrast, QT 25 sample predominantly exhibits cleavage fracture with also several intergranular facets (Figure 7(g)). During stable crack propagation, the fracture mechanism of the Q & P steels becomes more ductile with more dimples, while the tempered martensitic steel (QT 25) shows similar fracture surface at crack initiation and during tearing.

IV. DISCUSSION

A. Effect of Quenching Temperature on Microstructure and on Tensile Properties

According to Koistinen–Marburger relationship (Figure 1), the amount of RA decreases with a decrease

in quenching temperature (Figure 3). In addition, the amount and size of blocky RA are reduced because of an increase in the amount of martensite (Figures 2(a), (c), and (e)). At the same time, film RA between martensitic laths becomes the predominant morphology (Figures 2(e) and (f)). The UTS × TE product tends to increase with an increase in the RA content. This is consistent with earlier studies.^[10,26] It is well known that continuous transformation of RA to martensite during uniaxial tension contributes to a large and sustained strain hardening exponent (Figure 4(c)), resulting in a large UTS × TE product (such as 24,993 MPa pct obtained with QT 211 sample in Table I). Similarly, Fe-0.42C-1.46Mn-1.58Si-0.028Nb (wt pct) Q & P steel having 16 pct RA has a high strain hardening exponent (up to 0.108) and, in turn, a large UTS × TE product (31,400 MPa pct).^[27] Due to very limited amount of RA (0.5 pct) in tempered martensitic steel (QT 25), the strain hardening exponent continuously decreases (Figure 4(c)), resulting in poor UE (3.55 ± 0.15 pct) and TE (8.10 ± 0.30 pct). However, the high fraction of

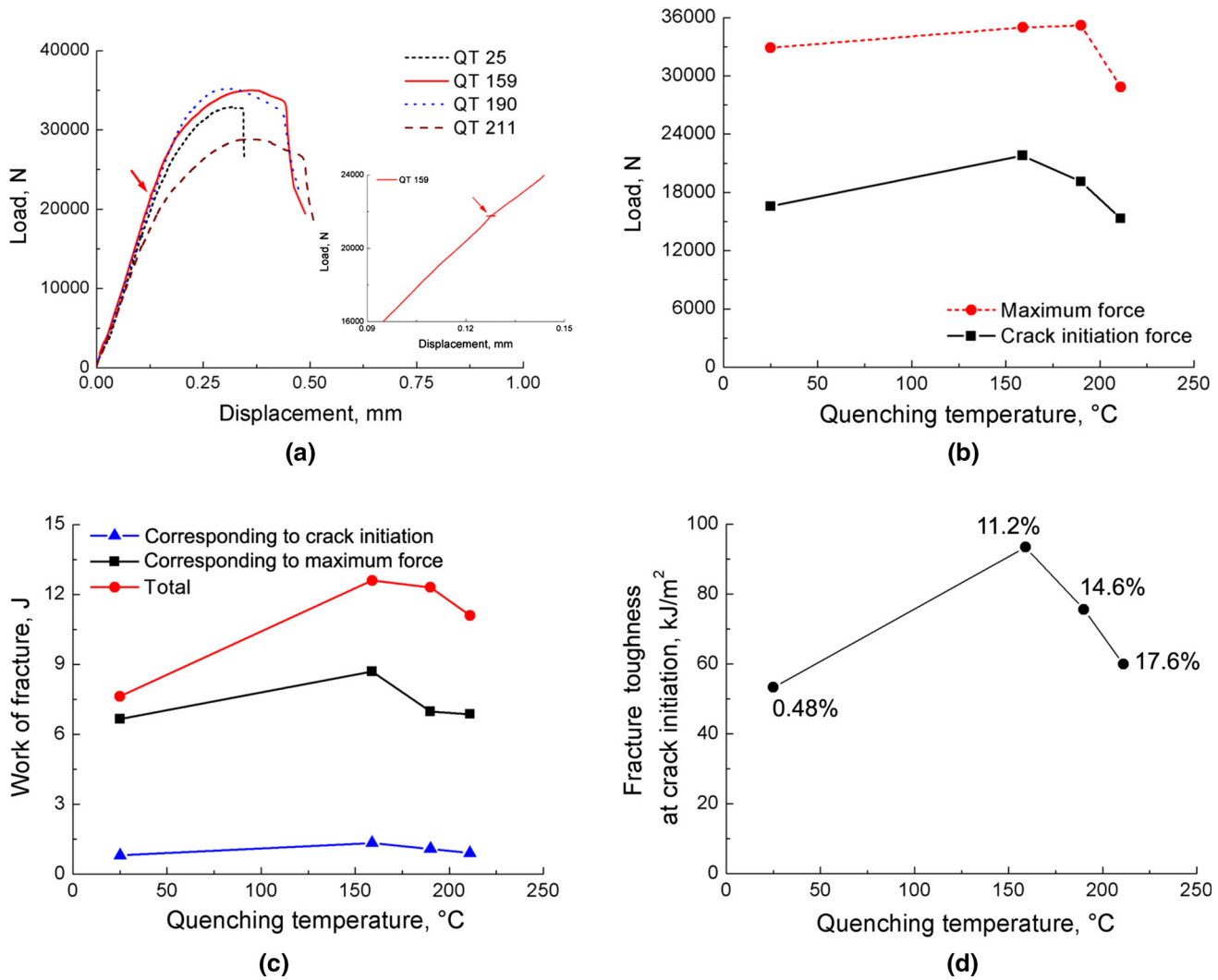


Fig. 6—(a) Load–displacement curves, (b) crack initiation force and maximum force, (c) work of fracture, and (d) fracture toughness at crack initiation as a function of quenching temperature. The corresponding volume fraction of retained austenite is indicated in (d).

martensite leads to a very high UTS up to 1631 ± 17 MPa.

A decrease in the amount of blocky RA (Figure 2) leads to a decrease in UE (Table I and Figure 4(b)) since blocky RA predominantly transforms to martensite before necking.^[28] Interestingly, the QT 159 sample has a higher TE but a smaller UE than QT 190 sample (Table I). In comparison with the QT 190 sample (Figures 2(c) and (d)), a smaller amount of blocky RA in the QT 159 sample (Figures 2(e) and (f)) leads to a smaller UE. Generally, film RA has a higher stability than blocky RA and, in turn, it predominantly transforms at larger strains (typically after the onset of necking).^[29,30] As a result, it largely contributes to work hardening at large strain.^[28] Although QT 190 sample has a larger fraction of RA (14.6 pct) than QT 159 sample (11.2 pct), higher fraction of blocky RA is in the former and, in turn, they probably exhibit similar volume fraction of film RA. Moreover, Figure 3 shows higher RA carbon content in the QT 159 sample compared to QT 190 sample (0.98 vs 0.95 wt pct) and the size of film RA in QT 159 sample is much finer (*cf.*

Figures 2(c), (d) and (e), (f)). Smaller RA grain size leads to a higher stability.^[31,32] Thus, finer film RA with higher carbon content in QT 159 sample contributes more to strain hardening in the large strain regime compared to QT 190 sample, leading to a larger TE. Noticeably, an increased RA content in Q & P steels leads to a continuous increase in ϵ_f and the $\sigma_f \times \epsilon_f$ product (Table I). One possible reason is that the transformation of RA to martensite enhances the strain hardening ability which delays void coalescence (Figures 5(a) through (c)).^[33,34] In contrast, tempered martensitic steel has the largest ϵ_f and the largest $\sigma_f \times \epsilon_f$ product (Table I) probably because of delayed void nucleation. Void nucleation on small carbides (Figure 5(d)) is known to require large plastic deformation.^[35]

B. The Role of Retained Austenite in Fracture Resistance

The UTS \times TE product deteriorates with a decrease in RA content (Table I), while the fracture resistance is enhanced in terms of the work of fracture (Figure 6(c))

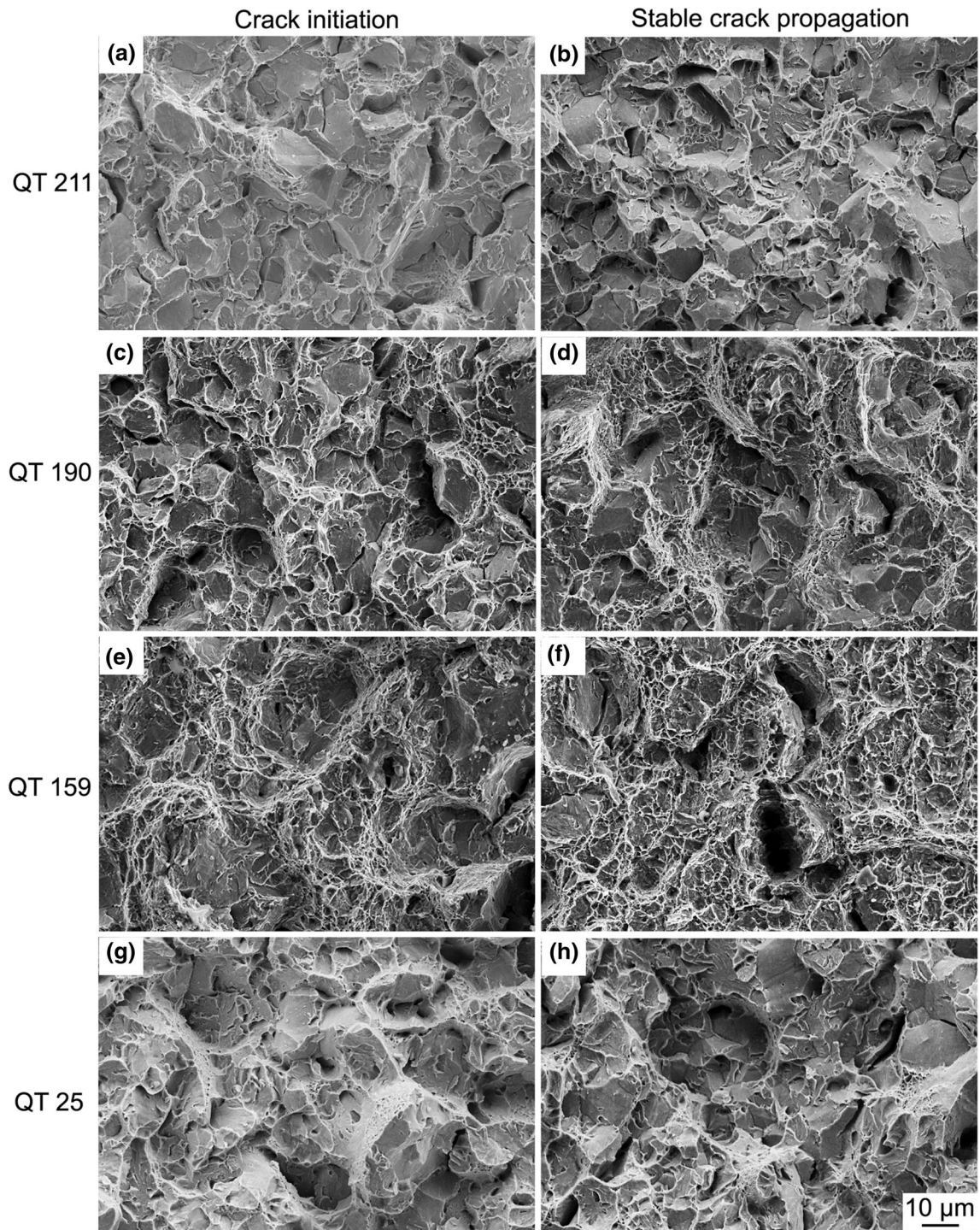


Fig. 7—Fracture surfaces at (a, c, e, g) crack initiation (adjacent to the initial notch tip) and (b, d, f, h) during stable crack propagation ($\sim 400 \mu\text{m}$ away from the initial notch tip) of different DENT samples: (a, b) QT 211, (c, d) QT 190, (e, f) QT 159, and (g, h) QT 25.

and of the fracture toughness at crack initiation (Figure 6(d)). This phenomenon, as shown in Figure 8(b), is opposite to the common view that a large $\text{UTS} \times \text{TE}$ product indicates a high fracture resistance. Efthymiadis *et al.*^[15] also demonstrated that a higher TE did not ensure a higher fracture resistance by studying the dependence of fracture resistance on tensile properties in DP steels and CP steels. Instead, the

difference in hardness between different phases should be considered and the YS–UTS ratio could be used as a criterion.^[15] Moreover, there is no clear relationship between fracture toughness at crack initiation J_{Ic} and the $\sigma_f \times \varepsilon_f$ product (Figure 8(c)). It is mainly because of different fracture modes observed in the studied steels under different loading configurations. Under uniaxial tension condition, ductile fracture is dominant

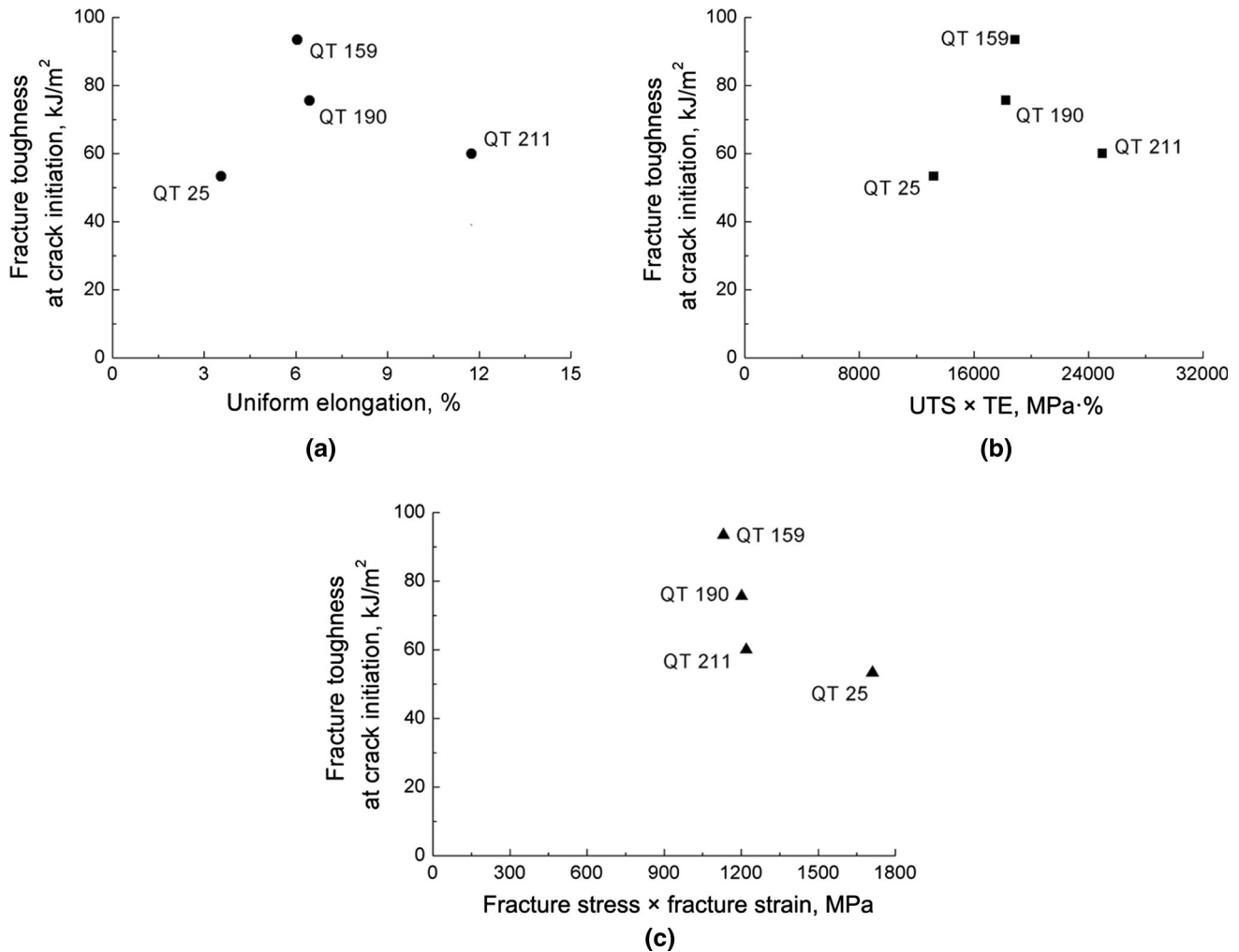


Fig. 8—Fracture toughness at crack initiation as a function of (a) uniform elongation, (b) the product of ultimate tensile strength and total elongation, and (c) the product of fracture stress and fracture strain.

(Figure 5), whereas DENT test with pre-cracks leads to cleavage fracture in the QT 25 sample, intergranular fracture in the QT 211 and QT 190 samples, and ductile fracture in the QT 159 sample (Figure 7). Remarkably, the fracture toughness of these samples correspondingly increases in the same order. As a conclusion, uniaxial tensile tests considering global deformation along the whole gauge length cannot be used as an indicator of cracking resistance from pre-existing defect, while fracture toughness should be considered.

In comparison with uniaxial tension, the RA also plays an important but different role when undergoing the loading associated to a near crack tip region. RA will transform to martensite at a much higher rate in the fracture process zone of the DENT specimens due to the higher stress triaxiality.^[20,36] This has been recently demonstrated by the present authors.^[36] As it can be seen in QT 211 sample (Figures 2(a) and (b)), many blocky RA grains decorate the boundaries of martensitic packets. After these RA grains have quickly transformed to martensite, fresh martensite is distributed in the form of a brittle necklace along martensitic packet boundaries. Fresh martensite cannot effectively

accommodate deformation of the matrix and in turn promotes crack formation.^[37] It will easily lead to crack propagation along the brittle fresh martensite, resulting in an intergranular fracture mode (Figure 7). Similarly, although the microstructure is finer and RA content is slightly smaller in QT 190 sample than in QT 211 sample, the former still has many blocky RA islands along the martensitic packet boundaries (Figures 2(c) and (d)), leading to an intergranular fracture mode as well (Figure 7). Nevertheless, with a decrease in quenching temperature down to 159 °C (QT 159) and, in turn, in the RA fraction down to 11.2 pct (Figure 3), the predominant morphology of RA in QT 159 sample turns to be film shaped between martensitic laths (Figures 2(e) and (f)). This breaks the necklace distribution of blocky RA islands along the martensitic packet boundaries and, in turn, results in a dominant ductile fracture mode consisting of dimples even in a pre-cracked specimen (Figure 7). The low fraction of blocky RA-to-martensite transformation does not allow intergranular fracture and offers a chance for void nucleation at the interface of fresh martensite and even at cracked martensite,^[38] leading to the formation of

dimples in fracture surfaces. This change in RA morphology from blocky to film type significantly enhances fracture toughness from 60.0 (QT 211) to 93.4 (QT 159) kJ m^{-2} (Figure 6(d)).

The crack initiation/maximum force and the corresponding work of fracture decrease with an increase in RA fraction (Figures 6(b) and (c)) since larger RA fraction (namely, brittle fresh martensite after transformation) requires smaller stress for crack initiation.^[39] Importantly, the QT 211 sample has a small crack initiation/maximum force (15.3/28.8 kN) even lower than tempered martensitic steel (QT 25, 16.5/32.9 kN), indicating the adverse effect of necklace blocky RA on the resistance to crack initiation and propagation. However, QT 211 sample exhibits a slightly higher fracture toughness at crack initiation (60.0 kJ m^{-2}) compared to the QT 25 sample (53.3 kJ m^{-2}). This small difference presumably comes from the counterbalance between the assistance of fresh martensite (transformed from RA) to induce crack initiation and the energy consumption by RA-to-martensite transformation. Nevertheless, the total work of fracture in Q & P steels is significantly larger in comparison with tempered martensitic steel (QT 25, Figure 6(d)), clearly showing the contribution of RA-to-martensite transformation to crack propagation resistance.^[40] A final point of interest regarding the cracking process is that intergranular propagation is stable when it occurs (Figure 6(a)), which is different from usual brittle type intergranular process. This is due to the fact that the intergranular damage requires to proceed that the RA gets transformed first into martensite; hence, it requires that sufficient amount of plasticity keeps being generated in the fracture process zone while the crack is moving forward.

C. Compromise Between Tensile Properties and Fracture Resistance

Usually, formability is mainly related to high UE. This is a valid engineering practice in most low- to medium-strength alloys where formability is often dictated by plastic localization. However, in high-strength alloys, resistance to cracking from defects produced by sheet cutting is also an issue. Thus, both sufficiently large UE (> 6 pct based on industrial practice) and sufficiently high J_{Ic} are required at the same time in AHSSs. With an increased RA fraction in the studied two-step Q & P steels (Figure 3), UE increases (Figure 4(d)) but the fracture resistance decreases (Figure 6(d)). An excellent performance in the tensile behavior is achieved due to TRIP effect when the RA fraction is large. Compared with uniaxial tension condition, the much higher stress triaxiality in DENT test markedly enhances the transformation rate of RA, leading to the early formation of percolating brittle fresh martensite network. When the blocky RA islands distribute along the boundaries of martensitic packets (such as QT 211 sample in Figures 2(a) and (b)), the

formation of fresh martensite necklace significantly deteriorates the fracture resistance through a change of fracture mode to intergranular fracture (Figure 7). When the film RA becomes dominant instead of the blocky type, the fracture resistance is significantly improved but the UE is reduced (Figure 8(a)). Therefore, for enhancing the balance between tensile properties and fracture resistance, a control of the amount and morphology of RA should be considered in order to keep large UE and avoid easy crack nucleation and propagation because of the “brittle necklace” effect.

V. CONCLUSION

The mechanical response of two-step Q & P steels with chemical composition 0.3C-2.5Mn-1.5Si-0.8Cr (wt pct) was studied for different quenching temperatures. The uniaxial tension properties and the cracking resistance were evaluated using uniaxial tension and pre-crack DENT tests, respectively, leading to the following conclusions:

- (1) When decreasing the quenching temperature from 211 °C to 159 °C, the RA fraction decreases from 17.6 to 11.2 pct and the predominant morphology of RA changes from blocky to film type, leading to a decrease in the $UTS \times TE$ product by 27 pct. This is ascribed to the decreasing impact of the TRIP effect.
- (2) In QT 211 and QT 190 conditions, the fracture mode in uniaxial tension is ductile. In contrast, fracture is intergranular in the DENT specimens. The origin of this transition into an intergranular fracture mode results from early formation of fresh martensite in the fracture process zone due to the high stress triaxiality, which is transformed from blocky RA grains distributed along the boundaries of martensitic packets.
- (3) In comparison with the deterioration in tensile properties, the fracture resistance is enhanced with a decreased RA content in Q & P steels. This is due to the continuous elimination of blocky RA islands decorating the boundaries of the martensitic packets. To optimize both the fracture toughness and tensile properties, a simultaneous control of the morphology and of the amount of RA is required.
- (4) Q & P steels show better fracture resistance than tempered martensitic steel, indicating a positive contribution from RA-to-martensite transformation.

The present study shows that a direct relationship between uniaxial tensile properties and fracture toughness cannot be made. As a general methodological conclusion, the present study, proves, once again, that it is very dangerous to generate conclusions about the cracking resistance of an alloy based only on uniaxial tension evidences.

ACKNOWLEDGMENTS

This work was funded by ArcelorMittal Global R&D Maizières Products in France.

REFERENCES

1. J. Speer, D. Matlock, B. de Cooman, and J. Schroth: *Acta Mater.*, 2003, vol. 51, pp. 2611–22.
2. M.J. Santofimia, L. Zhao, R. Petrov, C. Kwakernaak, W.G. Sloof, and J. Sietsma: *Acta Mater.*, 2001, vol. 59, pp. 6059–68.
3. J. Mola and B.C. de Cooman: *Scripta Mater.*, 2011, vol. 65, pp. 834–37.
4. J.G. Speer, D.V. Edmonds, F.C. Rizzo, and D.K. Matlock: *Curr. Opin. Solid State Mater. Sci.*, 2004, vol. 8, pp. 219–37.
5. D. Edmonds, K. He, F. Rizzo, B. de Cooman, D. Matlock, and J. Speer: *Mater. Sci. Eng. A*, 2006, vol. 438, pp. 25–34.
6. E. Ariza, M. Masoumi, and A. Tschiptschin: *Mater. Sci. Eng. A*, 2017, vol. 713, pp. 223–33.
7. Y. Toji, H. Matsuda, M. Herbig, P. Choi, and D. Raabe: *Acta Mater.*, 2014, vol. 65, pp. 215–28.
8. J. Speer, E. De Moor, and A. Clarke: *Mater. Sci. Technol.*, 2005, vol. 31, pp. 3–9.
9. P. Huyghe, L. Malet, M. Caruso, C. Georges, and S. Godet: *Mater. Sci. Eng. A*, 2017, vol. 701, pp. 254–63.
10. E.J. Seo, L. Cho, Y. Estrin, and B.C. de Cooman: *Acta Mater.*, 2016, vol. 113, pp. 124–39.
11. F. HajyAkbar, J. Sietsma, G. Miyamoto, N. Kamikawa, R.H. Petrov, T. Furuhashi, and M.J. Santofimia: *Mater. Sci. Eng. A*, 2016, vol. 677, pp. 505–14.
12. E. De Moor, S. Lacroix, A. Clarke, J. Penning, and J. Speer: *Metall. Mater. Trans. A*, 2008, vol. 39A, pp. 2586–95.
13. Z.P. Xiong, A.G. Kostyryzhev, L. Chen, and E.V. Pereloma: *Mater. Sci. Eng. A*, 2016, vol. 677, pp. 356–66.
14. H. Mohrbacher: *Adv. Manuf.*, 2013, vol. 1, pp. 28–41.
15. P. Efthymiadis, S. Hazra, A. Clough, R. Lakshmi, A. Alamoudi, R. Dashwood, and B. Shollock: *Mater. Sci. Eng. A*, 2017, vol. 701, pp. 174–86.
16. D. Casellas, A. Lara, D. Frómeta, D. Gutiérrez, S. Molas, L. Pérez, J. Rehr, and C. Suppan: *Metall. Mater. Trans. A*, 2017, vol. 48A, pp. 86–94.
17. G. Lacroix, T. Pardoën, and P.J. Jacques: *Acta Mater.*, 2008, vol. 56, pp. 3900–13.
18. I. de Diego-Calderón, I. Sabirov, J. Molina-Aldareguia, C. Föjer, R. Thiessen, and R. Petrov: *Mater. Sci. Eng. A*, 2016, vol. 657, pp. 136–46.
19. R. Wu, W. Li, S. Zhou, Y. Zhong, L. Wang, and X. Jin: *Metall. Mater. Trans. A*, 2014, vol. 45A, pp. 1892–1902.
20. P. Jacques, Q. Furnemont, T. Pardoën, and F. Delannay: *Acta Mater.*, 2001, vol. 49, pp. 139–52.
21. S.M.C. van Bohemen: *Mater. Sci. Technol.*, 2012, vol. 28, pp. 487–95.
22. N. van Dijk, A. Butt, L. Zhao, J. Sietsma, S. Offerman, J. Wright, and S. van der Zwaag: *Acta Mater.*, 2005, vol. 53, pp. 5439–47.
23. J. Rice, P.C. Paris, and J.G. Merkle: *ASTM STP*, 1973, vol. 536, pp. 231–45.
24. T.L. Anderson: *Fracture Mechanics: Fundamentals and Applications*, 4th ed., CRC Press, Boca Raton, 2017.
25. M.K. Hatami, T. Pardoën, G. Lacroix, P. Berke, P.J. Jacques, and T.J. Massart: *J. Mech. Phys. Solids*, 2017, vol. 98, pp. 201–21.
26. Z.P. Xiong, A.G. Kostyryzhev, A.A. Saleh, L. Chen, and E.V. Pereloma: *Mater. Sci. Eng. A*, 2016, vol. 664, pp. 26–42.
27. K. Zhang, P. Liu, W. Li, Z. Guo, and Y. Rong: *Mater. Sci. Eng. A*, 2014, vol. 619, pp. 205–11.
28. E.V. Pereloma, A.A. Gazder, and I.B. Timokhina: *Encyclopedia of Iron, Steel and Their Alloys*, Taylor and Francis, Inc., New York, 2016, pp. 3088–3103.
29. Z.P. Xiong, A.A. Saleh, R.K.W. Marceau, A.S. Taylor, N.E. Stanford, A.G. Kostyryzhev, and E.V. Pereloma: *Acta Mater.*, 2017, vol. 134, pp. 1–15.
30. S. Zhang and K.O. Findley: *Acta Mater.*, 2013, vol. 61, pp. 1895–1903.
31. W. Li, H. Gao, H. Nakashima, S. Hata, and W. Tian: *Mater. Charact.*, 2016, vol. 118, pp. 431–37.
32. D. de Knijf, C. Föjer, L.A. Kestens, and R. Petrov: *Mater. Sci. Eng. A*, 2015, vol. 638, pp. 219–27.
33. A. Pineau, A. Amine Benzerga, and T. Pardoën: *Acta Mater.*, 2016, vol. 107, pp. 508–44.
34. T. Pardoën and J.W. Hutchinson: *J. Mech. Phys. Solids*, 2000, vol. 48, pp. 2467–2512.
35. D. Kwon and R.J. Asaro: *Metall. Trans. A*, 1990, vol. 21, pp. 117–34.
36. Z.P. Xiong, P.J. Jacques, A. Perlade, and T. Pardoën: *Scripta Mater.*, 2018, vol. 157, pp. 6–9.
37. Y. Li and T. Baker: *Mater. Sci. Technol.*, 2010, vol. 26, pp. 1029–40.
38. D. Tian, L.P. Karjalainen, B. Qian, and X. Chen: *JSME Int. J. A*, 1997, vol. 40, pp. 179–88.
39. J. Chen, Y. Kikuta, T. Araki, M. Yoneda, and Y. Matsuda: *Acta Metall.*, 1984, vol. 32, pp. 1779–88.
40. F. Matsuda, K. Ikeuchi, H. Okada, I. Hrivnak, and H. Park: *Q. J. Jpn. Weld. Soc.*, 1995, vol. 13, pp. 99–105.

Publisher's Note Springer Nature remains neutral with regard to jurisdictional claims in published maps and institutional affiliations.